Fuel Communications 19 (2024) 100117



Contents lists available at ScienceDirect

Fuel Communications

journal homepage: www.sciencedirect.com/journal/fuel-communications

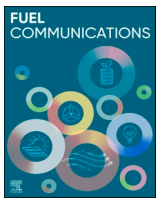



FGM vs ATF: A comparative LES analysis in predicting the flame characteristics of an industrial lean premixed burner for gas turbine applications

G. Lemmi [*,a], S. Castellani [a], P.C. Nassini [a], A. Picchi [a], S. Galeotti [a], R. Becchi [a], A. Andreini [a], G. Babazzi [b], R. Meloni [b]

[a] Department of Industrial Engineering, University of Florence, Via di Santa Marta 3, Florence, 50139, Italy
[b] Baker Hughes, Via F. Matteucci 2, Florence, 50127, Italy

ARTICLE INFO

Keywords:
Large Eddy Simulation
Artificially Thickened Flame model
Flamelet Generated Manifold
Industrial lean-premixed burner
Methane-air combustion modelling

ABSTRACT

In the pursuit of decarbonization, the reduction of greenhouse gas emissions from power generation through gas turbine (GT) engines plays a crucial role in the whole industrial sector. As industries strive to transition towards cleaner energy sources, the design and optimization of novel GT burners require a deep comprehension of the complex interaction between fluid dynamics and combustion processes embedded within the system. Computational Fluid Dynamics (CFD) plays a pivotal role in these processes by providing valuable insights into the complex flow patterns, flame topology, and stability limits within the combustor. Concurrently, the burner design phase necessitates a considerable number of simulations to ascertain flame stability limits under various burner designs and operating conditions. Therefore, it is imperative to control computational costs while ensuring a high level of accuracy. The present work is focused on a comprehensive comparative analysis of two widely employed turbulent combustion closure models: the Flamelet Generated Manifold (FGM) and the Artificially Thickened Flame (ATF). Both models utilize extended versions with specific modifications aimed at effectively addressing their respective limitations. The investigation is performed through a Large Eddy Simulation (LES) based CFD analysis within the context of a lean premixed burner designed by Baker Hughes and operated with methane at atmospheric pressure. The primary benchmark for numerical validation will be provided by detailed chemiluminescence images from a test campaign conducted by the University of Florence, thereby yielding valuable insights into flame topology and positioning. Furthermore, potential disparities in the flow field and fuel concentration at the burner exit between the two models will be revealed.

1. Introduction

In a global context where regulations on polluting emissions are progressively tightening [1], the quest for advanced technical solutions to mitigate the environmental impact of gas turbines poses a daunting challenge for industrial engineers. This endeavour demands a comprehensive understanding of the complex fluid dynamics and combustion processes inherent in the system. Within this challenge, Computational Fluid Dynamics (CFD) emerges as a key tool, providing invaluable insights into the flow field and flame topology within the burner, thereby supporting the understanding of its stability limits.

From a computational perspective, the imperative pursuit of an accurate mixing flow field stands as a fundamental step in accurately predicting the turbulent combustion dynamics. Retrieving the proper mixing flow field heavily relies on effectively addressing turbulence, highlighting the necessity to adopt scale-resolving CFD methods, with the LES approach predominating, particularly within the realm of industrial applications. In this context, although a substantial portion of turbulent kinetic energy is resolved within the computational grid, its interaction with the flame requires the application of a specialized combustion model.

Over the years, considerable effort has been dedicated to the development and validation of various turbulent combustion modelling approaches, including the Artificial Thickened Flame (ATF) [2], Flame Generated Manifolds (FGM) [3], G-equation [4,5], Flame Surface Density (FSD) [6], transport Probability Density Function (tPDF) [7], and Partially Stirred Reactor (PaSR) [8], among others [9,10]. However, a universal assessment of these combustion models proves challenging,

* Corresponding author.
E-mail address: gianmarco.lemmi@unifi.it (G. Lemmi).

https://doi.org/10.1016/j.jfueco.2024.100117
Received 23 November 2023; Received in revised form 5 April 2024; Accepted 5 April 2024
Available online 10 April 2024
2666-0520/© 2024 The Author(s). Published by Elsevier Ltd. This is an open access article under the CC BY-NC-ND license (http://creativecommons.org/licenses/by-nc-nd/4.0/).

Nomenclature

ATF	Artificially Thickened Flame
CFD	Computational Fluid Dynamics
DTFLES	Dynamic Thickened Flame model for Large-Eddy Simulations
FGM	Flamelet Generated Manifold
FR	Finite Rate
FSD	Flame Surface Density
FTT	Flow-Through-Time
HPC	High-Performance Computing
IRZ	Inner Recirculation Zone
LES	Large Eddy Simulation
LESIQ	LES Index Quality
ORZ	Outer Recirculation Zone
PaSR	Partially Stirred Reactor
PDF	Probability Density Function
PIV	Particle Image Velocimetry
RANS	Reynolds-Averaged Navier-Stokes
RMSE	Root Mean Square Error
THT	Technology for High Temperature
U.C.	University of California
UDF	User Defined Function

Symbols

a	Strain rate [s^{-1}]
c	FGM unnormalized reaction progress variable
D	Diffusion coefficient [$m^2\ s^{-1}$]
D_{th}	Thermal laminar flame thickness [m]
E	ATF model efficiency function
F	ATF model dynamic thickening factor
k	Turbulent kinetic energy [$m^2\ s^{-2}$]
M_i	Elemental mass of the i-species
n	Normal vector to the flame front
N_{thick}	Number of points within the thickened flame front
P	Static Pressure [Pa]
$P(x)$	PDF of the x-variable
S_l	Laminar flame speed [$m\ s^{-1}$]
u	Velocity x-component [$m\ s^{-1}$]
Y_i	Elemental Mass Fraction of the i-species
Z	Mixture fraction
Γ	Extended-FR correction factor
Γ_k	Extended-FR efficiency function
Δx	Mesh sizing [m]
δ_{ij}	Kronecker delta
ε	Dissipation rate of turbulent kinetic energy [$m^2\ s^{-3}$]
κ	Stretch [s^{-1}]
ν	Kinematic viscosity [$m^2\ s^{-1}$]
ρ	Density [$kg\ m^{-3}$]
σ_c	Curvature [s^{-1}]
ϕ	Progress variable variance
ψ	Extended-FR heat loss parameter
Ω	ATF model flame sensor
$\dot{\omega}_c$	Turbulent progress variable source term [s^{-1}]

Subscripts

res	Resolved quantity
sgs	Sub-grid scale modeled quantity
T	Turbulent quantity
$'$	Reynolds fluctuation
$''$	Favre fluctuation
-	Reynolds averaged
$\sim$	Favre averaged
o	Adiabatic unstrained

given their design-dependent performance and sensitivity to fuel composition. In this context, detailed experimental flame measurements play a crucial role in model validation, allowing designers to discern *when-and-how* a specific combustion model should take precedence over another, all while assessing computational costs. This requirement becomes particularly pronounced in the realm of real-scale geometries due to their complex features, always associated with high Reynolds numbers, thus demanding extensive computational domains for accurate turbulence resolution. Furthermore, the limited existing studies on industrial burners complicate the establishment of best practices for conducting numerical investigations into novel designs.

According to technical literature, two turbulent combustion models dominate the applications of LES to gas turbine burners: the tabulated-chemistry approach, where the FGM stands as the most widely adopted, and the ATF models [11] class. FGM is renowned for its computational efficiency, which arises from the decoupling of the reaction time scale from convection and diffusion processes, allowing for the pre-tabulation of the chemistry. Despite this, critical physical factors impacting the flame brush, such as stretch and heat loss, are not directly integrated into most common implementations and require customization [12]. In contrast, the ATF can naturally account for these aspects and, more importantly, address preferential diffusion, which is crucial for hydrogen combustion. The limitation of the latter model lies in its correct application solely to perfectly premixed mixtures. To extend the ATF to the treatment of non-premixed flames, a widely employed approach consists of disabling the artificial thickening on the diffusive flame front [13,14]. From a computational cost perspective, the ATF implies higher expenses, particularly with detailed or skeletal mechanisms, as it involves resolving a transport equation for each species in the employed reaction mechanism.

To overcome their respective limitations, this analysis employs extended versions of both models. Specifically, the dynamic thickened flame model for large-eddy simulations (DTFLES) [15,16] was selected for the ATF model, enabling the modelling of highly stratified combustion and accounting for spatial variations of flow and combustion metrics [17]. Regarding the FGM, the turbulence-chemistry interaction has been modelled through an extended version of the Finite-Rate approach that accounts for stretch and heat loss effects [18,19].

The focus of the present investigation centres on a comprehensive analysis of the aforementioned models by assessing their respective outcomes through an LES-based CFD approach on a GT lean-premixed combustor manufactured by Baker Hughes, operating with methane at atmospheric pressure. Detailed experimental measurements performed in the reactive test cell of the THT Lab of the University of Florence serve as a benchmark to compare the computational results provided by both the enhanced versions of the ATF and FGM. It is noteworthy that the local mesh sizings, tailored for the typical demands of industrial design applications, prompted the adoption of a slightly elevated thickening factor in the DTFLES model, a facet not commonly addressed in current literature, where academic test cases typically involve simpler geometries or significantly more demanding computational domains [20].

The investigated test rig conditions along with details of the computational domain will be presented in the subsequent section, which will be followed by a presentation of the mathematical formulations of the two enhanced models. The Results and Discussion section will then provide an in-depth comparison of the two models, addressing flame morphology, thermal, mixing, and velocity fields, while also delving into the merits and drawbacks of each model.

2. Experimental test rig

2.1. Burner geometry

Experiments are conducted in an optically accessible rig at the THT Lab of the University of Florence, featuring a state-of-the-art lean premixed burner designed by Baker Hughes specifically for heavy-duty gas turbine applications. The burner is supplied through two independent fuel lines [21], as illustrated in Fig. 1 (bottom) where the assembly of the main components of the dome is sketched. The main premixer injects fuel through a counter-rotating swirler, ensuring the delivery of a homogeneous mixture into the combustor. Conversely, the pilot line is responsible for the flame stabilization delivering the fuel gas directly into the primary zone. The combustion chamber has an internal diameter of 110 *mm* and an axial extension of approximately 2.5 diameters.

2.2. Tested operating conditions

Operated at atmospheric pressure, the rig utilizes natural gas as fuel at an inlet temperature of 300 *K*, while the combustor inlet air is set to 573 *K* for the reactive case, replicating typical gas turbine compressor discharge thermal conditions. The test cell operates with a constant air mass flow rate of 320 g/s injected through the plenum, including the component dedicated to liner cooling. The total fuel mass flow rate is adjusted to achieve a thermal power output of approximately 72 *kW*. Throughout the tests, the pressure drop across the combustion chamber, expressed as the differential pressure across the combustor over the combustor inlet pressure ($\Delta P/P$), was consistently around 4.2%. Additionally, the pilot split, defined as the ratio between the mass flow rate of fuel through the pilot line over the total one, is set to 30%.

2.3. Rig instrumentation

The rig is equipped with various thermocouples and static pressure probes to monitor the flow conditions. Flue gas composition is analyzed using a HORIBA PG-350 gas analyzer, with sampling occurring after approximately 9 *ms* of residence time to retrieve key pollutant emissions such as *CO* and NO_x. Regarding Particle Image Velocimetry (PIV) investigations, images were recorded through a Phantom MIRO M340 camera, with an acquisition frequency of 400 *Hz* for both cold and reactive tests. TiO_2 particles were introduced to seed the airflow directly upstream of the burner, and background noise was effectively removed through a dedicated algorithm. *OH** chemiluminescence measurements were conducted to assess flame topology for the given operating condition using the same camera as for PIV measurements and an intensifier equipped with a filter at 310 *nm*. Images are collected at 1000 *Hz*, with the gain and the gate set to 5 and 0.5 *ms*, respectively. For further details on the test rig, additional information can be found in the works of Babazzi et al. [22].

3. Numerical setup

The computational domain, outlined in Fig. 2, encompasses the entire burner geometry, ranging from the air plenum to the outlet section, incorporating features such as the double-swirler, fuel manifolds, effusion holes, and all the other features defining the full geometry of the combustor. A fully unstructured mesh comprising approximately 20 million polyhedral cells is employed, with various ad-hoc refinements determined through a preliminary mesh sensitivity analysis, which is not included here for brevity. In particular, due to the high velocity at the pilot jets exit and the necessity of accurately predicting the local mixing behaviour, an annular refined grid region with a local sizing of 240 μm is generated. Moreover, the double swirler region, as well as the main reaction zone within the chamber, presents a local refinement of 500 μm. This refinement aims to effectively resolve the high turbulence levels generated by the swirler and accurately predict the flow diffusion process upon entering the chamber. The same mesh configuration is maintained for both of the investigated combustion models.

All simulations are performed using the commercial pressure-based code ANSYS Fluent® 2022 R1, employing an unsteady high-fidelity LES approach. The effect of unresolved turbulence is addressed using the Dynamic Smogorinsky-Lilly formulation [23], which dynamically evaluates the Smagorinsky model parameter. The PISO algorithm [24,25] was adopted for the pressure-velocity coupling and set with a constant time-step of 5.0×10^{-6} *s* according to a maximum Courant number of 8 inside the domain. Second-order schemes were employed for both space and time discretization.

For all simulations, a constant mass flow rate of air and fuel is

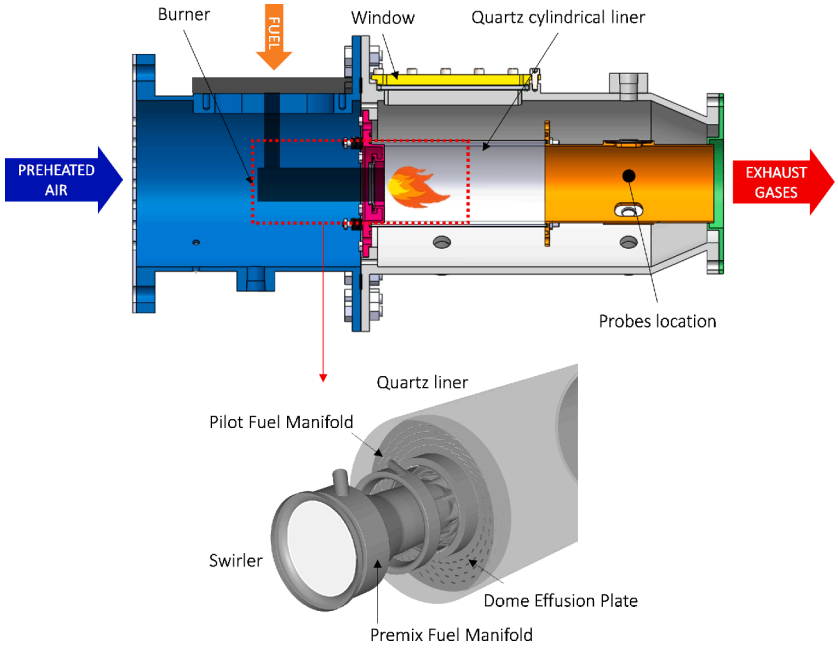

Fig. 1. Schematics of the THT Lab reactive test cell (top) [22] equipped with Baker Hughes lean-premixed burner (bottom).

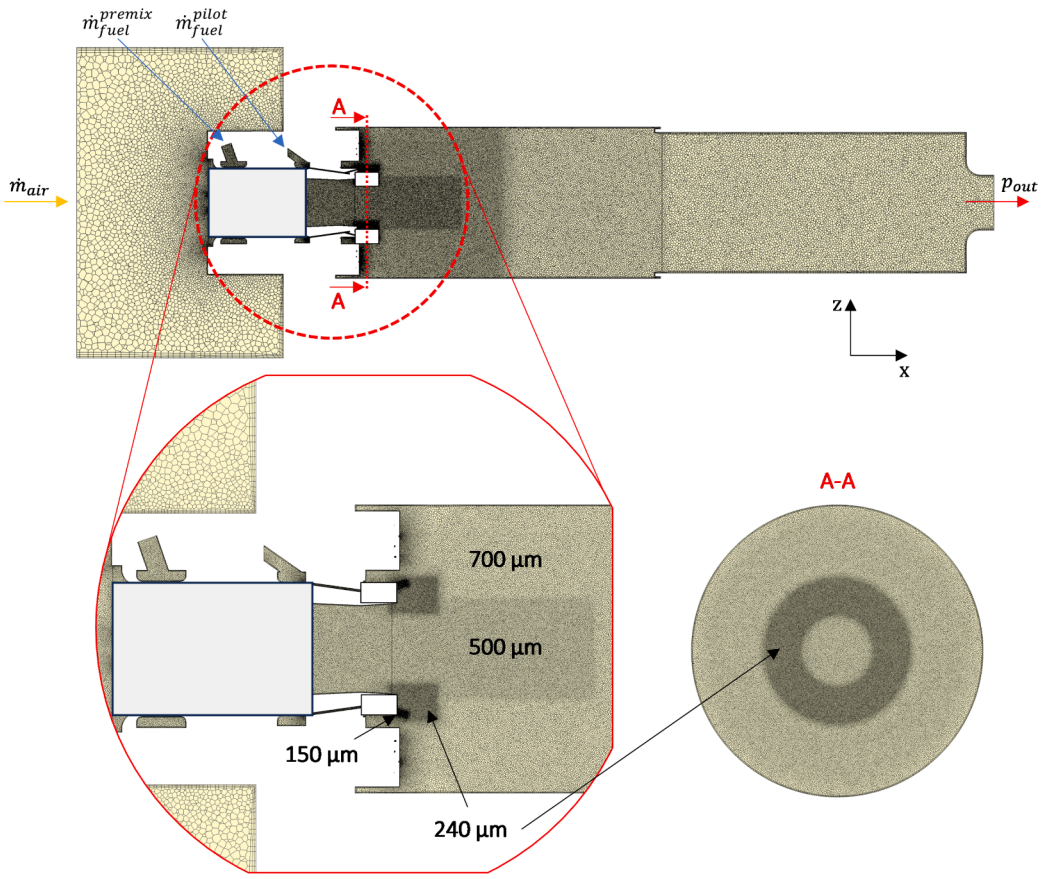

Fig. 2. Computational grid on a plane intersecting two axes of the pilot fuel line (midplane section). The mesh resolution is enhanced within the swirler and the primary zone regions, with its peak in the pilot fuel injection for a refined characterization of the mixing process. Design details omitted.

specified at the respective inlet patches based on the data presented in the previous section. Air humidity was not modelled, as no experimental measurements were conducted for this parameter. Concerning fuel composition, the experimental analysis revealed that Natural Gas consisted of 94% methane, 3% $C2+$ hydrocarbons, and the remaining 3% inert species. However, in the CFD simulations, the composition for both ATF and FGM was set as 100% methane. This decision was influenced by the limitations of the ATF model's reaction mechanism, which does not account for $C2+$ species, thereby containing the number of transport equations and reducing computational costs. The outlet is maintained at a constant atmospheric pressure, and, in this preliminary stage, the walls are treated as adiabatic with respect to thermal boundaries.

LES simulations using both ATF and FGM models are initiated from the solutions obtained in their respective preliminary reactive Reynolds-Averaged Navier-Stokes (RANS) simulations, with the latter employing the $k-\epsilon$ Realizable turbulence model. The LES simulations are then run for approximately 4 flow-through-times (FTT) and subsequently sampled for about 3 FTTs. Data are collected at a frequency corresponding to the chosen time step. To provide context, one FTT is estimated to be approximately 14 milliseconds.

4. Mathematical formulations of the tested combustion models

4.1. ATF:DTFLES

The ATF model, originally developed by Colin et al. [11] addresses challenges associated with the resolution of thin flame structures in high-fidelity turbulent combustion simulations. The chemistry-turbulence interaction is modified by artificially thickening the unresolved flame in order to obtain a new flame brush that can be directly resolved on the given grid resolution. In the dynamic version of the model [16], the flame thickening is achieved by introducing additional terms in the transport equation for species mass fractions and energy, including a dynamic thickening factor (F), a flame sensor (Ω), and an efficiency factor (E). According to Legier et al. formulation [15], the dynamic thickening factor is computed as:

$$F = \Omega(F_{max} - 1) + 1 \tag{1}$$

With F_{max} being the local maximum thickening factor, computed as a function of the local mixture composition and mesh sizing (Δx):

$$F_{max} = \frac{\Delta x N_{Thick}}{D_{th}} \tag{2}$$

Here, D_{th} is the thermal laminar flame thickness, tabulated as a function of the local mixture composition, and N_{Thick} is the user-specified number of grid points within the laminar flame thickness.

To prevent local mispredictions of fuel consumption in the flame front, distinguishing and modelling the premixed front separately from the diffusive front is essential. The approach outlined in [13] is applied in the present study to address this requirement. The Takeno flame index (ξ) [26] is employed to identify the cell-based combustion regime: for positive values, the original formulation is applied [11] with the flame thickness discretized through 9 mesh points. Alternatively, when the diffusive regime is detected, the flame front is not thickened and, consequently, a finite-rate closure is adopted. Additional details regarding this enhanced version of the ATF model can be found in the study conducted by Castellani et al. [14].

With the goal of minimizing the computational effort required by the DTFLES model employed for this investigation, a skeletal mechanism comprising 19 species and 62 reactions suitable for $CH_4 - H_2$ blends is retrieved from the detailed U.C. San Diego mechanism [27].

4.2. FGM: extended-FR

The FGM method falls within the flamelet model category [28], wherein the turbulence flame is described as a set of laminar flamelets i.e., locally 1D flames in which all variables are solely functions of mixture fraction Z and reaction progress variable c. According to Bilger [29], the mixture fraction is defined as follows [30]:

$$Z = \frac{0.5\left[\frac{Y_H - Y_{H,2}}{M_H}\right] + 2.0\left[\frac{Y_C - Y_{C,2}}{M_C}\right]}{0.5\left[\frac{Y_{H,1} - Y_{H,2}}{M_H}\right] + 2.0\left[\frac{Y_{C,1} - Y_{C,2}}{M_C}\right]} \tag{3}$$

Here, Y_H and Y_C are the elemental mass fractions of H and C in the measured sample, $Y_{H,1}$ and $Y_{C,1}$ the elemental mass fractions of H and C in the fuel inlet stream, $Y_{H,2}$ and $Y_{C,2}$ the elemental mass fractions of H and C in the oxidiser inlet stream, and M_H and M_C the elemental masses of H and C. The unnormalised progress variable is defined by default as $c = Y_{CO_2} + Y_{CO}$. In the preprocessing stage, a look-up table is generated by solving several laminar flamelets to describe thermodynamic quantities ($T, Y_i, \dot{\omega}_c, etc.$) as functions of the two independent control variables. The turbulence-chemistry interaction is accounted for by describing variables stochastically through the use of a joint mass-weighted β-shaped Probability Density Function ($\beta - PDF$) of Z and c, $\widetilde{P}(Z,c)$ [3]. Regarding the standard Finite Rate (FR), the turbulent progress variable source term ($\widetilde{\dot{\omega}}_c$) is computed as:

$$\widetilde{\dot{\omega}}_c(\widetilde{Z},\widetilde{c}) = \int\int \dot{\omega}_c(Z,c)P(Z,c)\,dZ\,dc \tag{4}$$

With $\dot{\omega}_c$ directly extracted from the laminar flamelets- look-up table. In this work, a transport equation for the reaction progress variable variance (ϕ) is used. According to ANSYS Fluent [30], the transport equation for ϕ is described by:

$$\vec{\nabla}\cdot(\bar{\rho}\widetilde{\vec{u}}\phi - \bar{\rho}(D+D_T)\vec{\nabla}\phi) = 2C_3\bar{\rho}D_T[\vec{\nabla}\widetilde{c}]^2 + 2C_4\overline{c''\dot{\omega}_c} - 2C_5\bar{\rho}\left(\frac{\varepsilon}{k}\right)\phi \tag{5}$$

In which C_3, C_4, and C_5 are modelling constants. The source term $\overline{c''\dot{\omega}_c}$ arises from the source term in the transport equation for the progress variable c and is defined as:

$$\overline{c''\dot{\omega}_c} = \overline{c\dot{\omega}_c} - \widetilde{c}\overline{\dot{\omega}_c} \tag{6}$$

Here, the Reynolds averaged source term $\overline{\dot{\omega}_c}$ is defined as:

$$\overline{\dot{\omega}_c} = \bar{\rho}\left(\widetilde{\frac{\dot{\omega}_c}{\rho}}\right) = \bar{\rho}\int\int \frac{\dot{\omega}_c(Z,c)}{\rho(Z,c)}\widetilde{P}(Z,c)dZdc \tag{7}$$

According to Eq. (4). Analogously, $\overline{c\dot{\omega}_c}$ is defined as:

$$\overline{c\dot{\omega}_c} = \bar{\rho}\int\int \frac{(c\dot{\omega}_c)(Z,c)}{\rho(Z,c)}\widetilde{P}(Z)\widetilde{P}(c)dZdc \tag{8}$$

For further insights into the mathematical structure of the FGM model, readers can refer to the work by Ramaekers et al. [30].

This study exploits an enhanced version of the conventional FGM approach, which incorporates the effects of flame stretch and heat loss in a pre-calculated table (Γ-table), thus directly impacting the combustion process reactivity. To achieve this, a new parameter (Γ) is defined and tabulated as a function of the strain rate (a) and heat loss (ψ), aimed at correcting the standard Finite Rate (FR) turbulent progress variable source term:

$$\widetilde{\dot{\omega}}_c(\widetilde{Z},\widetilde{c}) = \Gamma(a,\psi)\int\int \dot{\omega}_c(Z,c)P(Z,c)\,dZ\,dc \tag{9}$$

$\Gamma(a,\psi)$ is defined as the ratio between the maximum values of the strained, non-adiabatic progress variable source term and the adiabatic, unstrained one in a 1D laminar flame:

$$\Gamma(Z,c,a,\psi) = \frac{\max\dot{\omega}_c(Z,c,a,\psi)}{\max\dot{\omega}_c^0(Z,c)} \tag{10}$$

with ψ identifying the heat loss parameter, defined as the ratio between the burnt gas temperature and the corresponding equilibrium value, and a representing the strain, evaluated from the velocity flow field. It is worth noting that, in the specific case of this study, $\psi = 1$ due to the adiabatic thermal wall boundary condition characterizing this preliminary work. Cantera libraries are used to solve several freely propagating flames ($a = 0$) and premixed counterflow flames ($a > 0$) in order to generate the $\Gamma(a,\psi)$ table. In Fig. 3 the Γ table in Z and a space for the adiabatic condition ($\psi = 1$) is reported.

From the CFD side, flame stretch (κ) is computed using a User Defined Function (UDF) that employs an analytic expression based on three components: resolved strain ($\widetilde{a}_{res}$), sub-grid scale strain ($\widetilde{a}_{sgs}$), and curvature (σ_c). The expression is given by:

$$\kappa = \left(\delta_{ij} - \widetilde{n_i}\widetilde{n_j}\right)\frac{\partial\widetilde{u}_i}{\partial x_j} + \Gamma_\kappa\frac{\sqrt{k_{sgs}}}{\Delta} + S_l\frac{\partial\widetilde{n}_i}{\partial x_i} = \widetilde{a}_{res} + \widetilde{a}_{sgs} + \sigma_c \tag{11}$$

Here, δ_{ij} is the Kronecker delta, n is the normal vector to the flame front, Γ_κ is an efficiency function, k_{sgs} is the sub-grid kinetic energy, and S_l is the laminar flame speed. The normal vector to the flame front is computed from the resolved progress variable gradient:

$$n = \frac{\nabla\widetilde{c}}{\|\nabla\widetilde{c}\|} \tag{12}$$

Following the modelling strategy proposed by Tay Wo Chong [31], the sub-grid scale component of the strain ($\widetilde{a}_{sgs}$) is computed as a function of the sub-grid kinetic energy, the latter defined as follows:

$$k_{sgs} = \left(\frac{\nu_{sgs}}{\Delta}\right)^2 \tag{13}$$

An efficiency function is then used to correct the definition of the sub-grid scale strain, reducing the impact of the smallest eddies on flame stretch. In this work, the formulation proposed by Meneveau et al. [32] is employed:

$$\log_{10}\Gamma_\kappa = -\frac{1}{s+0.4}e^{-(s+0.4)} + \left(1 - e^{-(s+0.4)}\right)(s\sigma - 0.11) \tag{14}$$

$$s = \log_{10}\left(\frac{\Delta}{\delta_l^0}\right), \qquad \sigma = \frac{2}{3}\left(1 - \frac{1}{2}\exp\left[-\left(\frac{u'_\Delta}{S_c^0}\right)^{\frac{1}{3}}\right]\right) \tag{15}$$

Here, δ_l^0 and S_c^0 identify the unstretched laminar flame front

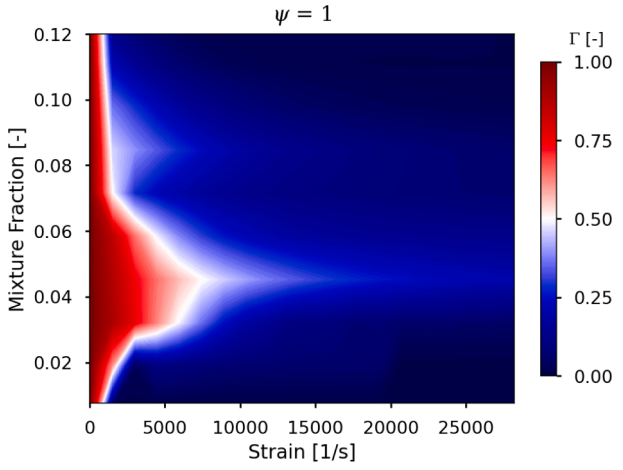

Fig. 3. Γ table in the mixture fraction and strain space for the adiabatic condition ($\psi = 1$).

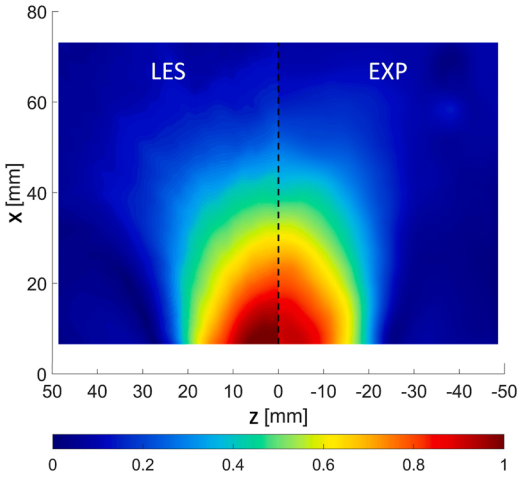

Fig. 4. Normalised time-averaged velocity magnitude on the $z-x$ plane of the LES simulation (left) compared to the PIV experimental data (right).

thickness and consumption speed, respectively, with u'_{Δ} the sub-grid velocity fluctuation.

According to Eq. (11), the impact of stretch on the flame front is computed as the combined effect of strain and curvature. It is crucial to underscore that the impact of stretch on the flame is solely dependent on the magnitude of this combined effect, and the apportionment of strain and curvature does not affect it. This enabled the utilization of strained flamelets - i.e., premixed counterflow flames - as a representative for both strain and curvature in generating the gamma table.

The heat loss is computed as the ratio of the local temperature to the local adiabatic temperature. Further details regarding this enhanced version of the FGM are available in [18,19]. The detailed GRI-Mech 3.0 [33], involving 53 species and 325 elementary chemical reactions, was employed as the reaction mechanism for generating the look-up table.

5. Results and discussion

In this section, the main outcomes of the numerical study carried out on Baker Hughes' industrial burner are presented. The numerical investigation serves a dual purpose: firstly, it validates the implemented models (turbulence, combustion, etc.), and secondly, it facilitates an in-depth exploration of the underlying physics governing observed phenomena. Significantly, CFD allows for the examination of the mixing process by extracting the mixture fraction field, a parameter that cannot be obtained through experimental means. Consequently, the comparative analysis between CFD results and experimental data not only contributes to model validation but also enhances the interpretation of experimental outcomes, thereby providing a deeper understanding of the studied processes.

In the first part of this section, a validation of the numerical setup is conducted through a direct comparison of the computed flow field against experimental data under non-reactive and ambient conditions. Subsequently, a comparison between the ATF and FGM models is presented through an in-depth analysis of the key quantities describing the combustion process.

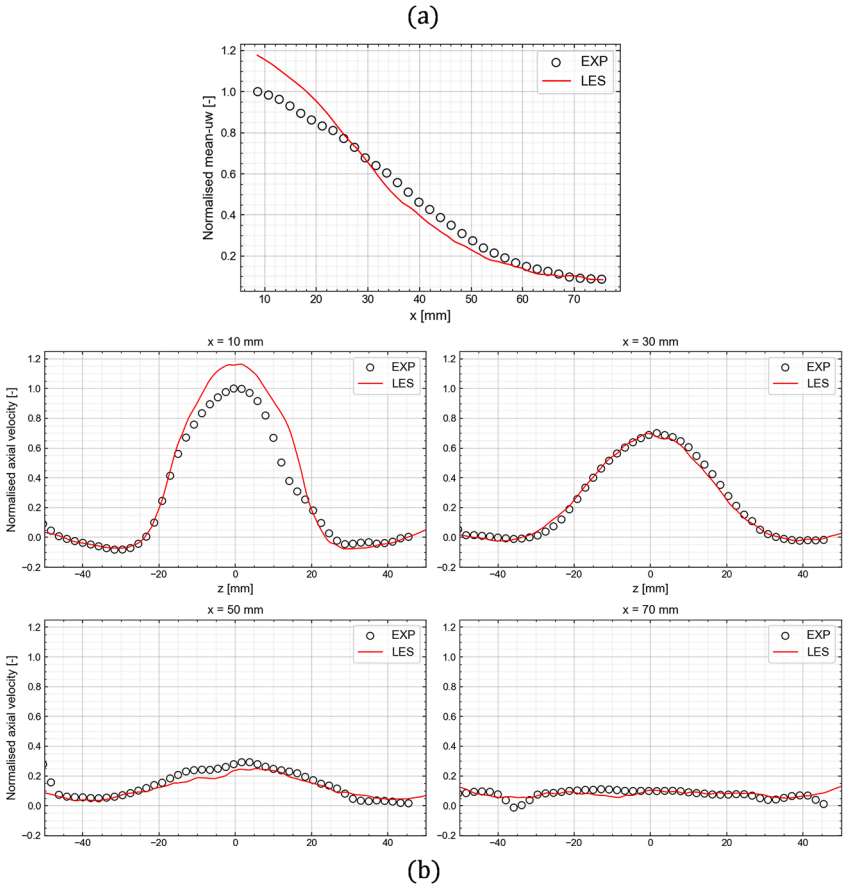

Fig. 5. Axial distribution of normalised time-averaged velocity magnitude on the along the axis of simmetry of the burner (*a*); radial distributions of normalised time-averaged axial-velocity at different axial coordinates (*b*): a comparison between LES results and PIV data.

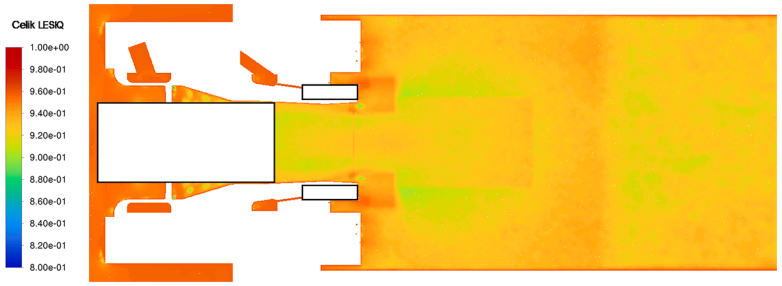

Fig. 6. Contour plot illustrating the time-averaged Celik LESIQ on the $z - x$ plane of symmetry of the burner. The highest values are predominantly observed within the mesh-refined zones surrounding the pilots.

5.1. Numerical Setup validation: cold flow field

The first analysis was carried out under non-reactive conditions, utilizing pure air as the working fluid set at ambient pressure and temperature conditions. The primary objective of this phase was to validate the computational setup. Fig. 4 shows a qualitative comparison in terms of mean velocity magnitude on the $z - x$ plane between the computed results and the PIV experimental data. The numerical setup accurately predicts the flow field, although a noticeable overprediction in the axial-velocity peak is observed. This discrepancy might be attributed to the potential presence of noise or laser partial reflection within the entry region of the chamber (i.e., dome) that could have affected the local accuracy of the PIV measurements. This observation is supported by both axial and radial profiles of mean axial velocity displayed in Fig. 5, where numerical results closely align with the experimental data starting from a distance of 20 *mm* from the dome. A pressure drop of 4.2% between the inlet and outlet of the burner was computed, showing perfect alignment with the experimental measurements.

Finally, an assessment of the LES resolution utilized in this study is reported. Specifically, the LES quality index proposed by Celik [34] is employed. This metric is defined as follows:

$$LESIQ = \frac{1}{1 + 0.05\left[\frac{(\nu+\nu_{SGS})}{\nu}\right]^{0.53}} \tag{16}$$

where the value of *LESIQ* ranges between 0 and 1. In Fig. 6, a contour map of the Celik LES quality index is presented. The time-averaged values of LESIQ consistently exceed 0.92, endorsing the grid resolution employed in this work.

Based on the results obtained with the presented numerical configuration, the setup was considered validated for use in the reactive case.

5.2. Reactive case: mixing and velocity field

In this second part of this section, the validated numerical setup is employed to conduct a reactive simulation under the conditions presented in Section 2.2.

As previously mentioned, to ensure efficient combustion, a homogeneous fuel-oxidizer mixture within the chamber is achieved by the presence of a dual counter-swirling premixer. The mixing field is depicted in Fig. 7, where normalized time-averaged contours of mixture fraction and the corresponding root mean square error (RMSE) values on the domain midplane are depicted. It is noteworthy that, for the ATF model, the mixture fraction is computed from species following Eq. (3). The normalised mean mixture fraction plot at the premixer-chamber interface (section B-B) shows the presence of a uniformly mixed composition across a big part of the cross-sectional area of the premixer, with the strongest gradient located in the proximity of the walls. Section A-A, instead, underscores the impact of the swirled flow on the diffusion of the fuel injected from the pilots.

The efficacy of the employed premixer in achieving a uniformly mixed composition within the primary zone is further substantiated by the nearly exhaustive identification of a premixed flame regime, the latter determined through an analysis of the Takeno flame index from the ATF model simulation. For clarification, Fig. 8 displays the instantaneous map of the product between the normalized Takeno flame index and fuel consumption. Positive values are associated with a premixed regime, whereas negative values are indicative of a diffusive one. Despite a confined area around the pilots exhibiting a non-premixed regime, the flame predominantly operates under premixed conditions.

Transitioning to the analysis of the flow field, Fig. 9 presents the normalised time-averaged axial velocity alongside the RMSE of velocity magnitude contour maps on a longitudinal plane of the burner. The inclusion of RMSE provides a comprehensive assessment of turbulence levels within the domain. The highlighted iso-line of zero velocity identifies the outer recirculation zone (ORZ), contributing to the generation of the shear layer around the pilots and thereby promoting flame stabilization. This observation finds further support in Fig. 10, illustrating both time-averaged mixture fraction and planar velocity fields within the primary zone, where the ORZ aligns with the isoline of the mixture fraction peak. In contrast, the presence of two smaller recirculation zones at the corners is associated with effusion cooling injection. Noteworthy is the absence of an inner recirculation zone (IRZ) due to the low swirl number characterizing the burner.

In comparing the ATF and FGM models, the flow fields within the combustion chamber exhibit strong agreement between the two numerical approaches, with only minor discrepancies. As depicted in Fig. 10, along the centerline ($z = 0$) corresponding to the main region, the ATF model exhibits a more axially developed fluid region outside the main burner characterized by higher mixture fraction values compared to the FGM model. Conversely, in the pilot region, the zone with higher mixture fraction values appears to be shorter for the ATF model. These observations suggest that in the ATF model, the pilot flame mainly enriches the main region rather than the recirculation zone. This interpretation is further supported by Fig. 11, where radial distributions of the normalized time-averaged mixture fraction, alongside axial velocity and their respective RMSE, at various distances from the dome are presented. In particular, at a distance of 10 *mm* from the dome, the plots emphasize a marginally higher mixture fraction peak for the FGM around the pilot region, whereas the ATF model maintains a slightly greater value around the core region throughout a big portion of the axial development of the burner.

With regard to the flow field, minimal distinctions are discernible in the axial velocity distribution between the two models, except for a slightly enhanced diffusion process evident in the ATF model around the burner axis. This distinction is noticeable in the plots at 30 and 50 *mm* from the dome, where the FGM model maintains higher axial velocity values at $z = 0$.

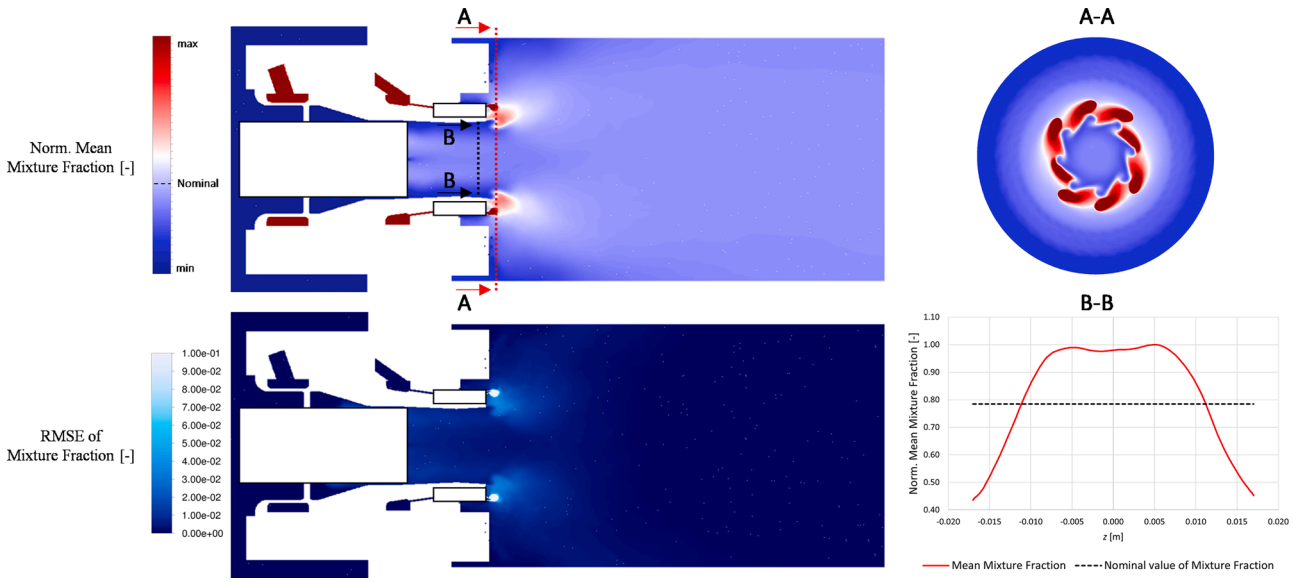

Fig. 7. Normalized time-averaged contours of Mixture Fraction on the $z-x$ plane of symmetry of the burner and a cross-sectional plane of the primary zone (top). Additionally, a z-axis distribution on the premixer-chamber interface and the RMSE contour on the midplane are included for detailed analysis.

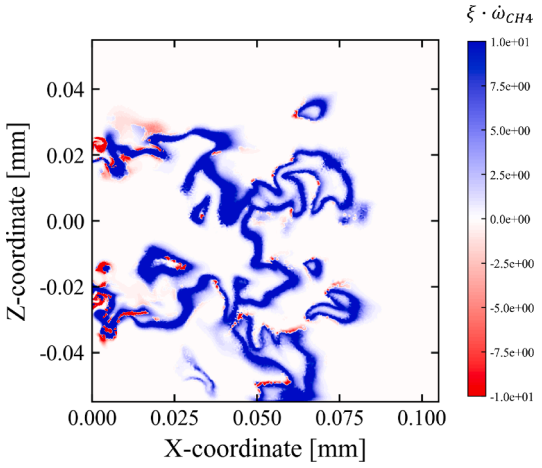

Fig. 8. Instantaneous contour of the normalised Takeno flame index on a longitudinal $z-x$ plane multiplied for the fuel consumption for better visualisation. The blu regions are associated with a premixed regime (positive values), while the red zones to a non-premixed one (negative values).

5.3. Reactive case: flame topology and thermal field

The prediction of the flame shape and position of the two numerical models against the experimental measurements is reported in Fig. 12.

The experimental data comprises the Abel-deconvoluted *OH** signal acquired from a camera placed orthogonally to the combustor axis and is compared with the time-averaged contour plots of heat release on the midplane. To facilitate an effective visual comparison between computed and experimental results, only half of the domain is displayed. The peak of heat release aligns closely with the shear layer surrounding the pilot jets, consistent with the mixture fraction distribution. Significantly, the pilots assume a crucial role in enhancing flame stabilization by enriching the flame anchoring point on the surface.

Overall, both combustion models exhibit reasonable predictions of the flame topology: the FGM shows a slight overprediction of the heat release peak region compared to the ATF, meaning that the former approach is affected by a higher reactivity around the pilot jets. Conversely, at the flame tip, the FGM tends to underestimate the local heat release, while the ATF aligns more closely with the experimental OH* intensity map. Despite both models being able to identify the main flame stabilization around the pilot jets, experiments reveal a slightly

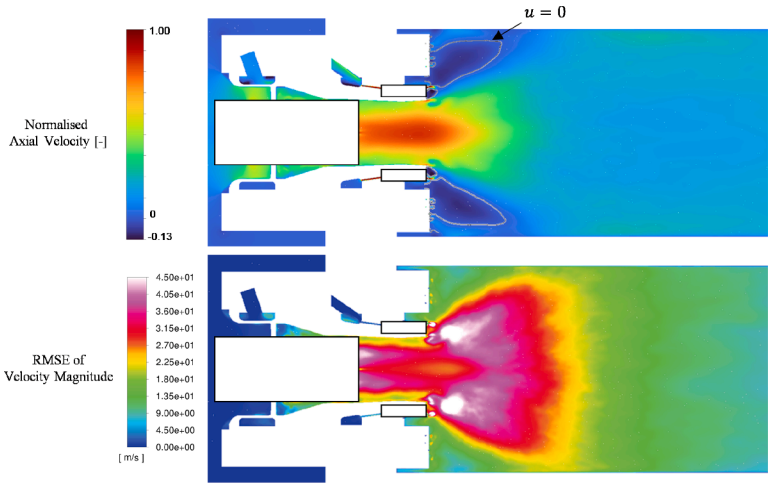

Fig. 9. Normalised time-averaged axial velocity field and RMSE of velocity magnitude map on a longitudinal plane of the burner.

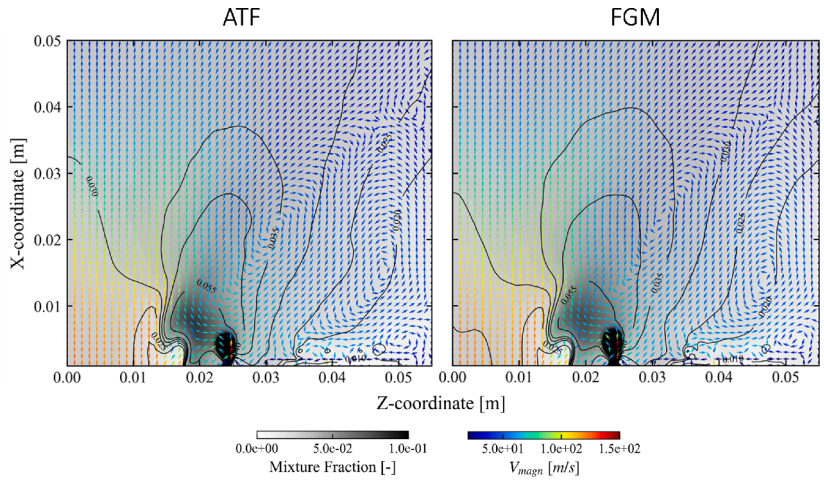

Fig. 10. Time-averaged mixture fraction field and planar velocity vector-plot on a longitudinal plane within the primary zone for both the numerical models.

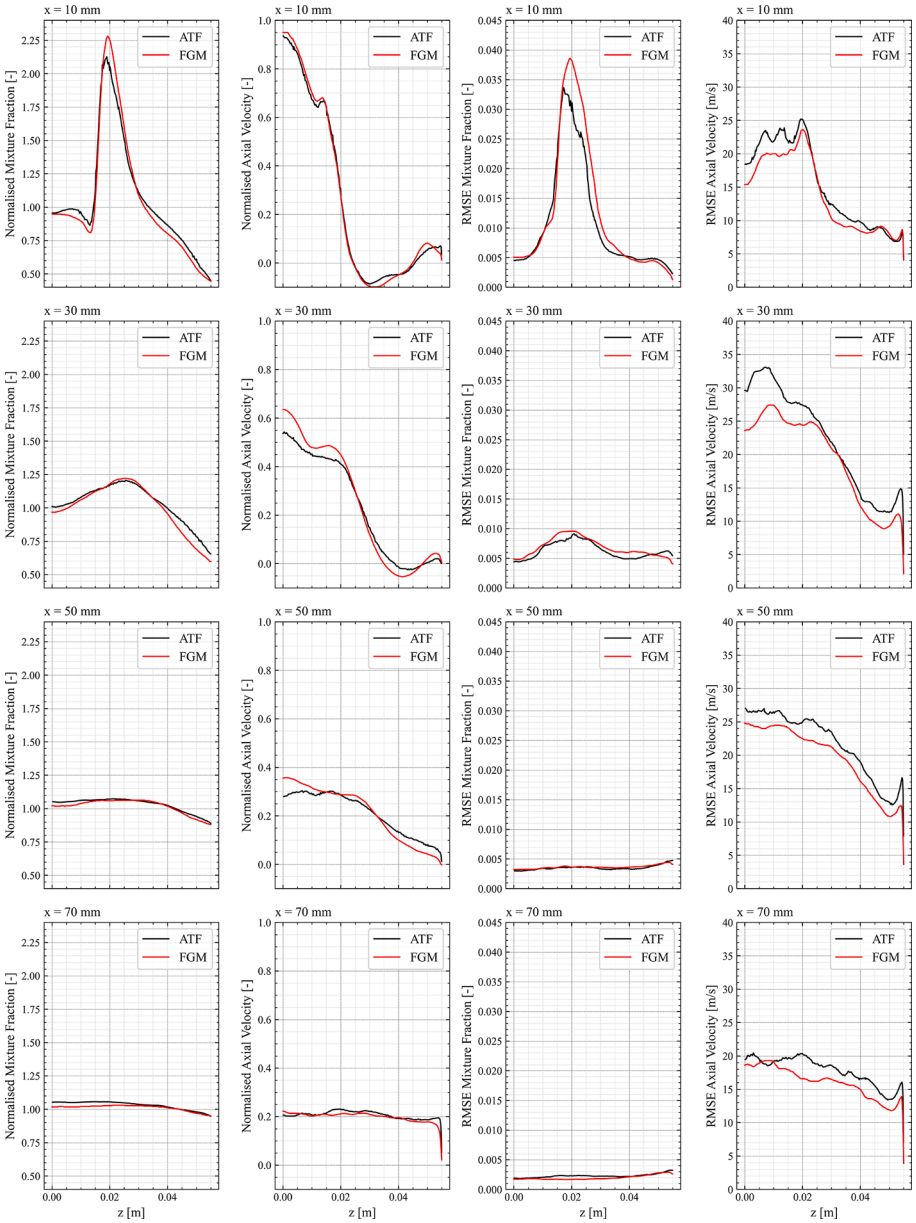

Fig. 11. Radial distributions of normalised time-averaged mixture fraction (first column) and axial velocity (second column) alongside their respective RMSE (third and fourth column) at different axial coordinates: a comparison between ATF and FGM computed results.

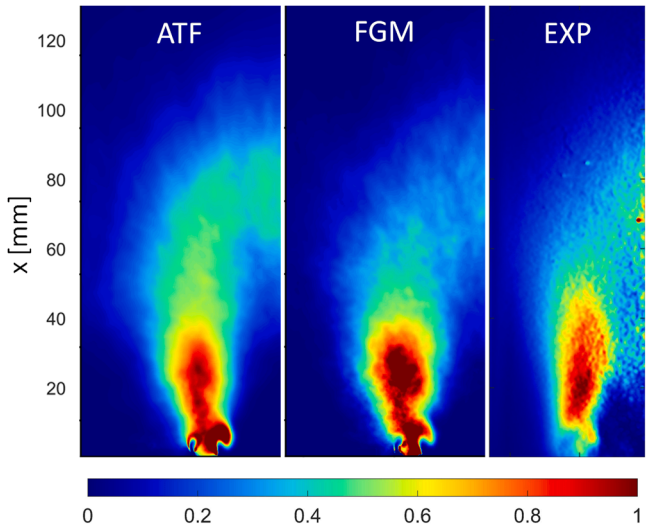

Fig. 12. Normalised time-averaged heat release rate from the ATF (left) and the FGM (centre) compared with the Abel-deconvoluted *OH** from the test (right).

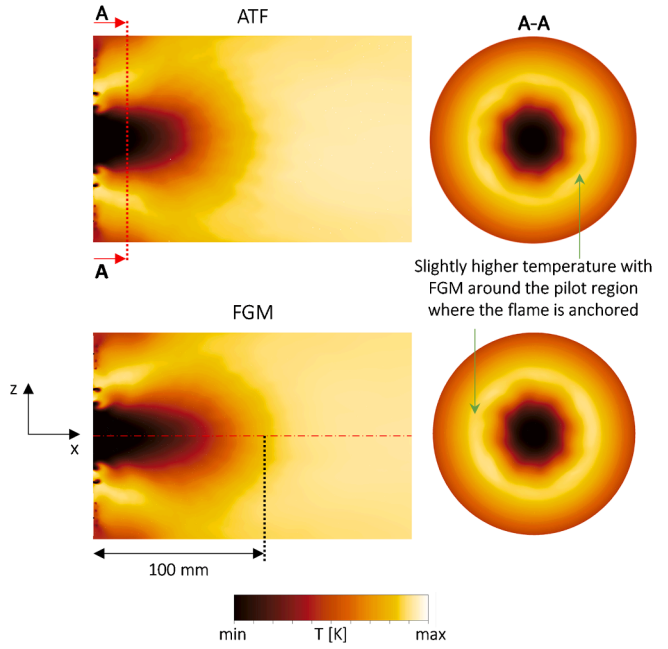

Fig. 13. Time-averaged temperature field in a longitudinal and a transversal plane within the primary zone for both the numerical models. The axial distance from the dome is provided as a reference, enhancing clarity for subsequent radial temperature distributions.

more lifted flame. In contrast, the computed heat release displays a secondary peak downstream of the pilot fuel injection. This observation is likely influenced by the adiabatic thermal boundary condition imposed on the burner wall of both models, adopted due to the unavailability of direct wall temperature measurements at that position.

The thermal field within the chamber demonstrates strong agreement between the two combustion models, as depicted in Fig. 13, where contour plots of time-averaged temperature in longitudinal and cross-sectional planes within the primary zone of the flame tube are presented. Investigating minor distinctions, both locations reveal a slightly higher peak temperature for the FGM model compared with the ATF throughout the pilot-stabilized region, coherently with the previously identified locally higher heat release. This discrepancy has the potential to impact the prediction of pollutant emissions, especially for NO_x. On the other hand, the FGM exhibits a slightly longer low-temperature region, following the locally lower heat release affecting the tip of the flame.

The discernible trend is prominently depicted in the plots of Fig. 14, showcasing radial (z direction) distributions of normalized time-averaged temperature at various axial coordinates. The zero radial coordinate aligns with the chamber axis. Particularly, the distributions at 50 and 70 *mm* from the dome clearly show the lower temperature affecting the flame tip of the FGM. Despite this localized difference, the overall temperature fields predicted by the two models exhibit remarkable uniformity. The absence of notable differences in both heat release and temperature fields between the two models suggests that any deviations from experimental results cannot be attributed specifically to turbulent combustion modelling. Rather, common elements in both numerical setups, such as local domain discretization or boundary conditions, may be influencing the observed discrepancies.

To delve deeper into the ATF model simulation details, a snapshot of the thickening factor is presented in Fig. 15. The contour illustrates the thickening factor just before the application of the flame index-based disabling criterion. Examination of the maximum thickening factor values reveals a consistent maintenance below 10, with the highest values concentrated near the pilot jets, outside the mesh refinement region. In these areas, the mixture enrichment from the pilot jets results in a remarkably thin laminar flame thickness, below the mesh size, leading to an increase in the thickening factor, as depicted in Fig. 15 (left). Conversely, in regions proximate to the pilot exit, the thickening requirements are relaxed due to the decrease in the mesh size. In this latter region, the flame exhibits a multi-regime nature, and the thickening factor is disabled based on the flame index value. The resolution of the diffusive part of the flame front is entirely entrusted to the local grid, thus justifying the considered requirements of a very fine mesh for that specific region.

5.4. Computational costs

All simulations presented in this study were conducted on an HPC cluster equipped with 20 multi-core Intel® Xeon® Gold 6248 CPU nodes. On this hardware, the computational cost required for performing the entire simulation, including the time-averaging process, was estimated to be approximately 60,000 and 250,000 CPU hours for the FGM and ATF, respectively. This considerable discrepancy is attributed to the ATF's necessity to solve a transport equation for each species involved in the reaction mechanism. For the implemented skeletal version of the San Diego mechanism, this entails solving 19 equations, resulting in a total of 23 equations for the ATF, compared to the 5 equations for the FGM. Ultimately, this implies that the ATF incurs approximately four times the computational cost of an FGM, at least for the current methane-air combustion setup.

6. Conclusions

In this work, an assessment of the flame shape prediction of two enhanced versions of the FGM and ATF combustion models is performed through a direct comparison between the computed results and experimental data obtained from an in-house test rig. The numerical setup was preliminary validated by comparing the computed flow field against experimental data under non-reactive and ambient conditions. Regarding the reactive case, both models exhibit remarkable accuracy in predicting the flame topology. Notably, the primary differences between experimental measurements and numerical predictions emerge in the pilot jets region. The computational results indicate a second heat release peak just downstream of the pilot fuel injection, contrasting with the experimental observation of a slight local flame lift-off. Interestingly, the exclusion of wall heat losses from the analysis does not seem to have influenced the flame shape. Subsequent studies, although not detailed here, indicate a form of insulation of the flame behaviour from wall thermal boundary conditions, possibly due to a shielding effect of the

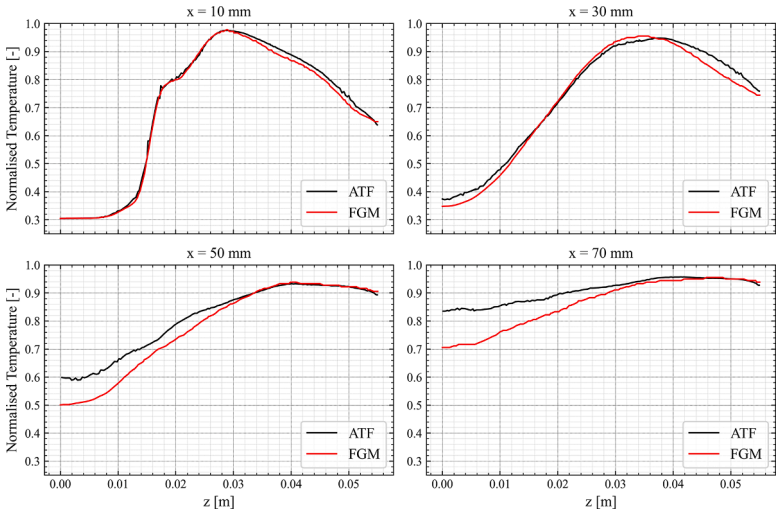

Fig. 14. Radial distributions of normalised time-averaged static temperature at different axial coordinates: a comparison between ATF and FGM computed results.

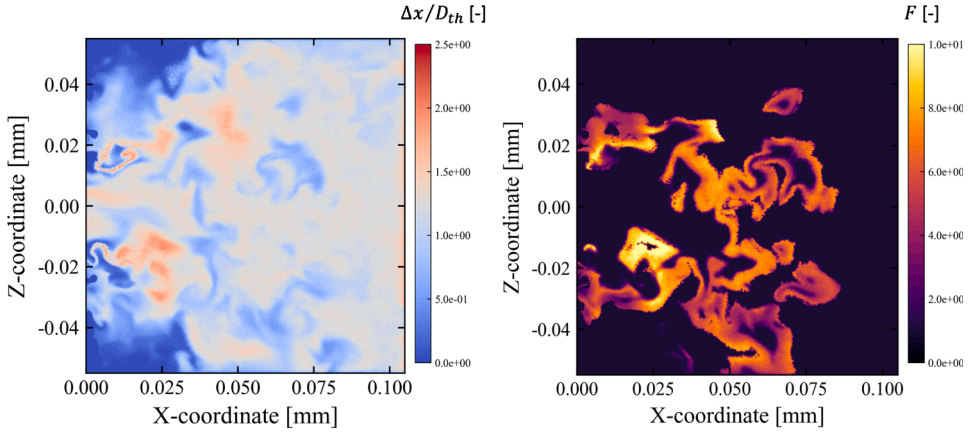

Fig. 15. Instantaneous contours of the ratio between the filter size and flame thickness (left) and the thickening factor (right) on a longitudinal $z-x$ plane of the burner.

effusion cooling against wall heat losses. Further investigations will delve into why neither model could capture the flame lift-off phenomenon observed during the experimental test campaign. On the other hand, both models exhibit a high degree of agreement with each other, suggesting that the local deviation with experimental results may be associated with measurement disturbances, local mesh sizings, or boundary conditions.

The accordance in the time-averaged heat release field between such diverse modelling approaches could be attributed to two factors: firstly, the flame heat release is primarily influenced by the mixing field, a prediction that relies less on the specifics of the combustion model and more on turbulence modelling. Secondly, the stretch and heat loss levels are not substantial enough to induce local flame extinctions, conditions under which differences between ATF and FGM might become more pronounced.

Nevertheless, the FGM has demonstrated its suitability for design-phase simulations by reasonably replicating the results from more computationally intensive models, such as the ATF.

CRediT authorship contribution statement

G. Lemmi: Data curation, Formal analysis, Investigation, Methodology, Validation, Visualization, Writing – original draft, Writing – review & editing. **S. Castellani:** Formal analysis, Supervision, Visualization, Writing – review & editing. **P.C. Nassini:** Resources, Supervision. **A. Picchi:** Supervision. **S. Galeotti:** Data curation, Supervision, Writing – review & editing. **R. Becchi:** Supervision. **A. Andreini:** Funding acquisition, Project administration, Resources, Supervision, Writing – review & editing. **G. Babazzi:** Supervision. **R. Meloni:** Conceptualization, Data curation, Investigation, Methodology, Project administration, Resources, Supervision, Writing – review & editing.

Declaration of competing interest

The authors declare that they have no known competing financial interests or personal relationships that could have appeared to influence the work reported in this paper.

Acknowledgements

The present research activity was carried out in the framework of TRANSITION (fuTure hydRogen Assisted gas turbiNeS for effective carbon capTure IntegratiON). This project has received funding from the Europen Union's Horizon Europe research and Innovation programme under Grant Agreement No 101069665. The Authors gratefully acknowledge this financial support.

Funded by the European Union

References

[1] Tsiropoulos DTI, Nijs W, Castello PR. Towards net-zero emissions in the eu energy system by 2050 - insights from scenarios in line with the 2030 and 2050 ambitions of the European green deal. EUR 29981 EN. Publications Office of the European Union; 2020. https://doi.org/10.3390/en14206694.

[2] Butler TD, O'Rourke PJ. A numerical method for two dimensional unsteady reacting flows. The Sixteenth (International) symposium on combustion. 1977. p. 1503–15.https://api.semanticscholar.org/CorpusID:263165939

[3] van Oijen J, Goey P. Modelling of premixed laminar flames using flamelet-generated manifolds. Combust Sci Technol 2000;161:113–37. https://doi.org/10.1080/00102200008935814.

[4] Williams FA. 3. Turbulent combustion. 1985. p. 97–131.

[5] Kerstein AR, Ashurst WT, Williams FA. Field equation for interface propagation in an unsteady homogeneous flow field. Phys Rev A 1988;37:2728–31. https://doi.org/10.1103/PhysRevA.37.2728.

[6] Hawkes E, Cant R. A flame surface density approach to large-eddy simulation of premixed turbulent combustion. Proc Combust Inst 2000;28(1):51–8. https://doi.org/10.1016/S0082-0784(00)80194-0.

[7] Haworth DC, Pope SB. Transported probability density function methods for Reynolds-averaged and large-eddy simulations. Dordrecht: Springer Netherlands; 2011. p. 119–42.ISBN 978-94-007-0412-1

[8] Péquin A, Iavarone S, Malpica Galassi R, Parente A. The partially stirred reactor model for combustion closure in large eddy simulations: physical principles, sub-models for the cell reacting fraction, and open challenges. Phys Fluids 2022;34(5):055122. https://doi.org/10.1063/5.0090970.

[9] Veynante D, Vervisch L. Turbulent combustion modeling. Prog Energy Combust Sci 2002;28(3):193–266. https://doi.org/10.1016/S0360-1285(01)00017-X.

[10] Echekki T, Mastorakos E. Turbulent combustion modeling: advances, new trends and perspectives. Fluid mechanics and its applications. Springer Netherlands; 2010.ISBN 9789400704114

[11] Colin O, Ducros F, Veynante D, Poinsot T. A thickened flame model for large eddy simulations of turbulent premixed combustion. Phys Fluids 2000;12(7):1843–63. https://doi.org/10.1063/1.870436.

[12] Klarmann N, Zoller B, Sattelmayer T. Numerical modeling of co-emissions for gas turbine combustors operating at part-load conditions. J Global Power Propuls Soc 2018;2:C3N5OA. https://doi.org/10.22261/JGPPS.C3N5OA.

[13] Aniello A, Laera D, Marragou S, Magnes H, Selle L, Schuller T, Poinsot T. Experimental and numerical investigation of two flame stabilization regimes observed in a dual swirl H2-air coaxial injector. Combust Flame 2023;249:112595. https://doi.org/10.1016/j.combustflame.2022.112595.

[14] Castellani S, Meloni R, Orsino S, Ansari N, Yadav R, Bessette D, Boxx I, Andreini A. High-fidelity H2-CH4 jet in crossflow modelling with a flame index-controlled artificially thickened flame model. Int J Hydrogen Energy 2023;48. https://doi.org/10.1016/j.ijhydene.2023.05.210.

[15] Legier J, Poinsot T, Veynante D. Dynamically thickened flame LES model for premixed and non-premixed turbulent combustion. Proc Summer Program 2000.

[16] Franzelli B. Impact of the chemical description on direct numerical simulation and large eddy simulation of turbulent combustion in industrial aero-engines. Institut National Polytechnique de Toulouse - INPT; 2011. Ph.D. thesis.

[17] Kazmouz S, Haworth D, Lillo P, Sick V. Extension of a thickened flame model to highly stratified combustion-application to a spark-ignition engine. Combust Flame 2022;236:111798. https://doi.org/10.1016/j.combustflame.2021.111798.

[18] Nassini PC, Pampaloni D, Meloni R, Andreini A. Lean blow-out prediction in an industrial gas turbine combustor through a LES-based CFD analysis. Combust Flame 2021;229:111391. https://doi.org/10.1016/j.combustflame.2021.02.037.

[19] Amerighi M, Nassini P, Andreini A, Orsino S, Verma I, Yadav R, Patil S. Assessment of flamelet generated manifold approach with inclusion of stretch effects of pure hydrogen flames. Proceedings of the ASME turbo expo 2023: turbomachinery technical conference and exposition. Turbo Expo: Power for Land, Sea, and Air, vol. 3A: Combustion, Fuels, and Emissions; 2023. https://doi.org/10.1115/GT2023-102651.

[20] Benard P, Lartigue G, Moureau V, Mercier R. Large-eddy simulation of the lean-premixed PRECCINSTA burner with wall heat loss. Proc. Combust. Inst. 2019;37(4):5233–43. https://doi.org/10.1016/j.proci.2018.07.026.

[21] Romano S, Meloni R, Riccio G, Nassini PC, Andreini A. Modeling of natural gas composition effect on low NOx burners operation in heavy duty gas turbine. J Eng Gas Turbines Power 2021;143. https://doi.org/10.1115/1.4049819.

[22] Babazzi G, Galeotti S, Picchi A, Becchi R, Cerutti M, Andreini A. Combustion diagnostics and emissions measurements of a novel low NOx burner for industrial gas turbine operated with CO2 diluted methane/air mixtures. Proceedings of the ASME turbo expo 2023: turbomachinery technical conference and exposition. Turbo Expo: Power for Land, Sea, and Air, vol. 3A: Combustion, Fuels, and Emissions; 2023. https://doi.org/10.1115/GT2023-101261.

[23] Lilly DK. A proposed modification of the Germano subgrid-scale closure method. Phys Fluids A Fluid Dyn 1992;4(3):633–5. https://doi.org/10.1063/1.858280.

[24] Issa R. Solution of the implicitly discretised fluid flow equations by operator-splitting. J Comput Phys 1986;62(1):40–65. https://doi.org/10.1016/0021-9991(86)90099-9.

[25] Issa R, Gosman A, Watkins A. The computation of compressible and incompressible recirculating flows by a non-iterative implicit scheme. J Comput Phys 1986;62(1):66–82. https://doi.org/10.1016/0021-9991(86)90100-2.

[26] Rosenberg DA, Allison PM, Driscoll JF. Flame index and its statistical properties measured to understand partially premixed turbulent combustion. Combust Flame 2015;162(7):2808–22. https://doi.org/10.1016/j.combustflame.2015.04.007.

[27] Chemical-kinetic mechanisms for combustion applications, San Diego mechanism web page, mechanical and aerospace engineering (Combustion Research). University of California at San Diego; 2016.(http://www.combustion.ucsd.edu)

[28] Peters N. Laminar flamelet concepts in turbulent combustion. Symp (International) Combust 1988;21(1):1231–50. https://doi.org/10.1016/S0082-0784(88)80355-2. Twenty-First Symposuim (International on Combustion)

[29] Bilger R, Stårner S, Kee R. On reduced mechanisms for methane-air combustion in nonpremixed flames. Combust Flame 1990;80(2):135–49. https://doi.org/10.1016/0010-2180(90)90122-8.

[30] Ramaekers W, Albrecht BA, van Oijen J, de Goey LPH. The application of flamelet generated manifolds in modelling of turbulent partially-premixed flames. Proceedings of the fluent benelux user group meeting. 1990. https://www.api.semanticscholar.org/CorpusID:166221911.3D–

[31] Tay-Wo-Chong L, Scarpato A, Polifke W. LES combustion model with stretch and heat loss effects for prediction of premix flame characteristics and dynamics. Proceedings of the ASME turbo expo 2017: turbomachinery technical conference and exposition. Turbo Expo: Power for Land, Sea, and Air, vol. 4A: Combustion, Fuels and Emissions; 2017. https://doi.org/10.1115/GT2017-63357.

[32] Meneveau C, Poinsot T. Stretching and quenching of flamelets in premixed turbulent combustion. Combust Flame 1991;86(4):311–32. https://doi.org/10.1016/0010-2180(91)90126-V.

[33] Frenklach M, Wang H, Goldenberg M, Smith G, Golden D, Bowman C, Hanson R, Gardiner W, Lissianski V. GRI-mech-an optimized detailed chemical reaction mechanism for methane combustion. Tech. Rep. Gas Research Institute Chicago; 1995.

[34] Celik IB, Cehreli ZN, Yavuz I. Index of resolution quality for large eddy simulations. J Fluids Eng 2005;127(5):949–58. https://doi.org/10.1115/1.1990201.